

# Global chemical weathering dominated by continental arcs since the mid-Paleozoic

Thomas Geron (✉ [Thomas.Geron@noc.soton.ac.uk](mailto:Thomas.Geron@noc.soton.ac.uk))

University of Southampton <https://orcid.org/0000-0002-7717-2092>

Thea Hincks

University of Southampton

Andrew Merdith

Claude Bernard University Lyon 1

Eelco Rohling

Australian National University <https://orcid.org/0000-0001-5349-2158>

Martin Palmer

University of Southampton

Gavin Foster

University of Southampton

Clement Bataille

University of Ottawa

R Dietmar Muller

The University of Sydney <https://orcid.org/0000-0002-3334-5764>

---

## Article

**Keywords:** Volcanic Outgassing, Silicate-rock Weathering, Weathering Flux, Bayesian Network, Continental Volcanic Arcs

**Posted Date:** November 19th, 2020

**DOI:** <https://doi.org/10.21203/rs.3.rs-91938/v1>

**License:**  This work is licensed under a Creative Commons Attribution 4.0 International License.

[Read Full License](#)

---

**Version of Record:** A version of this preprint was published at Nature Geoscience on August 23rd, 2021.  
See the published version at <https://doi.org/10.1038/s41561-021-00806-0>.

# Global chemical weathering dominated by continental arcs since the mid-Paleozoic

Thomas M. Gernon<sup>a,\*</sup>, Thea K. Hincks<sup>a</sup>, Andrew S. Merdith<sup>b</sup>, Eelco J. Rohling<sup>c</sup>, Martin R. Palmer<sup>a</sup>, Gavin L. Foster<sup>a</sup>, Clément P. Bataille<sup>d</sup>, R. Dietmar Müller<sup>e</sup>

<sup>a</sup>*School of Ocean & Earth Science, University of Southampton, Southampton SO14 3ZH, UK*

<sup>b</sup>*Laboratoire de Géologie, Université of Lyon 1, France*

<sup>c</sup>*Research School of Earth Sciences, The Australian National University, Canberra, Australia*

<sup>d</sup>*Earth and Environmental Sciences, University of Ottawa, Ottawa, ON K1N, Canada*

<sup>e</sup>*EarthByte Group, School of Geosciences, The University of Sydney, Australia*

## Summary

Earth's plate tectonic activity regulates the carbon cycle, and hence, climate, via volcanic outgassing and silicate-rock weathering<sup>1,2,3</sup>. Mountain building, arc-continent collisions, and clustering of continents in the tropics have all been invoked as controlling the weathering flux<sup>4,5,6</sup>, with arcs also acting as a major contributor of carbon dioxide (CO<sub>2</sub>) to the atmosphere<sup>7</sup>. However, these processes have largely been considered in isolation when in reality they are all tightly coupled. To properly account for the interactions between these processes, and the inherent multi-million-year time lags at play in the Earth system, we need to characterise their complex interdependencies. Here we analyse these interdependencies over the past 400 million years, using a Bayesian network to identify primary relationships, time lags and drivers of the global chemical weathering signal. We find that the spatial extent of continental volcanic arcs—the fastest-eroding surface features on Earth—exerts the strongest control on global chemical weathering fluxes. We find that the rapid drawdown of CO<sub>2</sub> tied to arc weathering stabilises surface temperatures over geological time, contrary to the widely held view that this stability<sup>8</sup> is achieved mainly by a delicate balance between weathering of the seafloor and the continental interiors.

1 Weathering of Earth's surface regulates climate<sup>1,3,4,9</sup>. When at- 24  
2 mospheric CO<sub>2</sub> concentrations are high and temperatures el- 25  
3 evated, these conditions lead to both ocean acidification and 26  
4 an intensified hydrologic cycle with increased evaporation, 27  
5 precipitation and runoff<sup>1</sup>. These conditions give rise to en- 28  
6 hanced weathering of silicate minerals and CO<sub>2</sub> drawdown. 29  
7 Conversely, reduced silicate weathering reduces CO<sub>2</sub> draw- 30  
8 down under cold climates, promoting warming. This 'thermo- 31  
9 stat' stabilises surface temperatures through time<sup>8</sup>. During the 32  
10 Phanerozoic (541–0 million years ago, Ma), the periodic on- 33  
11 set of icehouse conditions has variously been attributed to en- 34  
12 hanced weathering rates associated with mountain building<sup>4,10</sup>, 35  
13 reductions in continental arc magmatism<sup>7</sup>, and uplift of oceanic 36  
14 crust during arc-continent collisions<sup>5</sup>. Rather than occurring 37  
15 in isolation, these global tectonic processes are inextricably 38  
16 linked and the resulting collinearity—coupled with unknown 39  
17 time lags—obscures each process's individual contribution to 40  
18 global weathering fluxes. These issues have thus far severely 41  
19 limited our understanding of the first-order drivers of Earth's 42  
20 weathering fluxes.

## 21 Deep-time data mining

22 We constructed a deep-time Bayesian Network (BN) that 47  
23 uses data mining to systematically quantify the strength of the 48

relationships between key geological variables and the chem-  
ical weathering flux (Methods), and identify primary drivers  
and lags. To perform the analysis, we use UNINET, a soft-  
ware package for uncertainty analysis and high dimensional  
dependence modelling, originally developed for Civil Avia-  
tion Transport Safety (CATS). UNINET has proven capability  
for analysing complex data, and evaluating geological relation-  
ships and temporal dependencies<sup>17</sup>. We focus on the past 400  
million years (Myr), when key predictors of weathering flux  
such as crustal distribution, seafloor production rates<sup>11</sup> and at-  
mospheric CO<sub>2</sub><sup>12</sup> are best constrained (Fig. 1). The four main  
lineages of vascular plants had already proliferated on land by  
400 Ma<sup>18</sup>. This period encompasses the assembly and breakup  
of the Pangaea supercontinent (Fig. 1a), stable from ~320 to  
200 Ma (Fig. 1f). We compiled geospatial datasets using pale-  
ogeographic reconstruction from the open-source plate tectonic  
software *GPlates*<sup>19</sup>, processed in *R* (Methods), to produce a di-  
verse set of time series that capture times of key global tectonic  
changes (Fig. 1). Parameters include: continental arc length<sup>14</sup>;  
climate state (characterised by latitudinal extent of continental  
ice<sup>5</sup> and atmospheric CO<sub>2</sub> concentration<sup>12</sup>); suture zone length  
as a proxy for arc-continent collisions<sup>5</sup>; the spatial extent of  
large igneous provinces (LIPs)<sup>20</sup>; seafloor production rates; and  
continental fragmentation and dispersal (Fig. 1a, 1f).

We used variations in strontium isotope ratios in seawater  
(<sup>87</sup>Sr/<sup>86</sup>Sr)<sub>sw</sub> derived from marine carbonates<sup>15</sup> as a proxy  
for global chemical weathering through time, and calculated a

\*Corresponding author: Thomas.Gernon@noc.soton.ac.uk

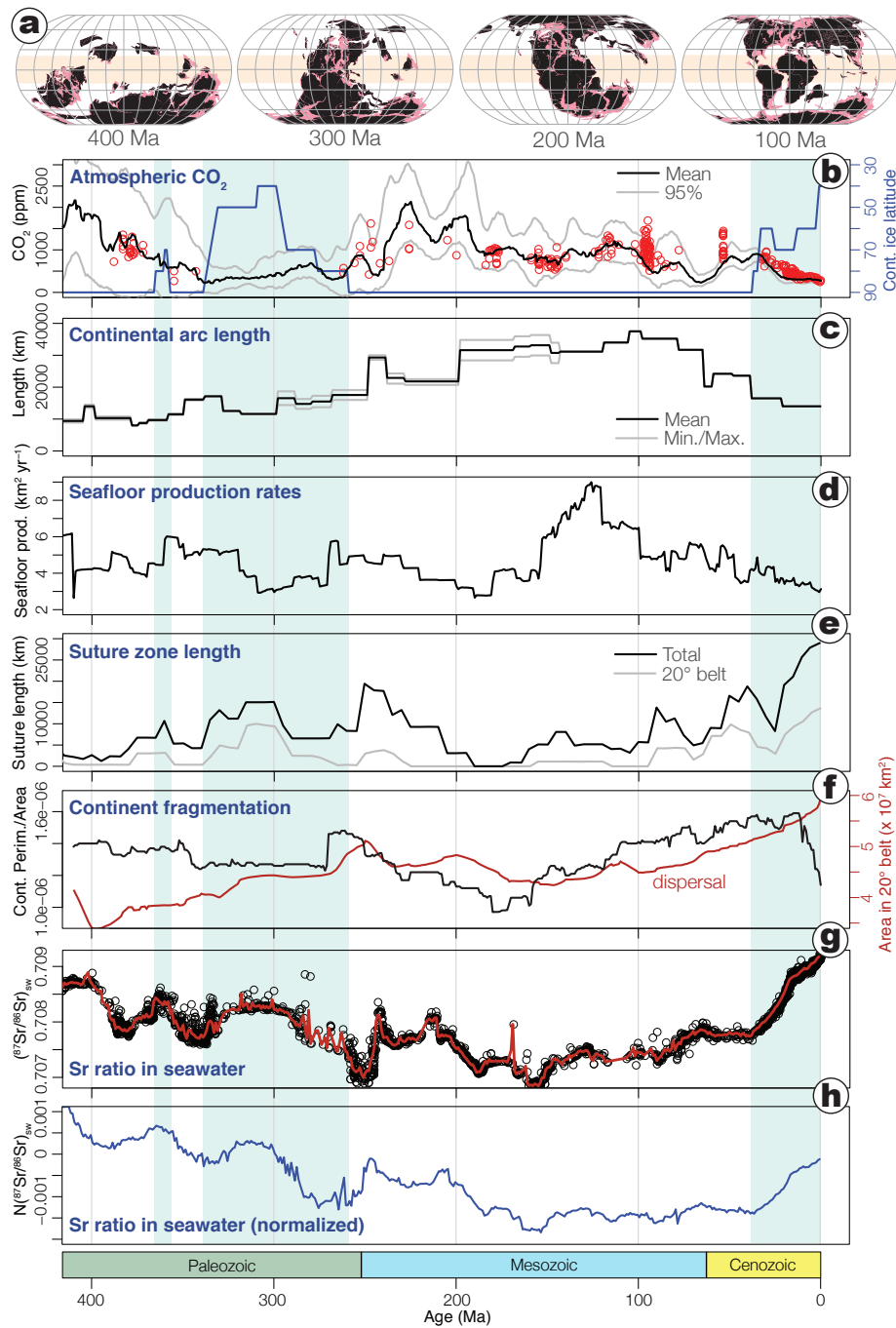


**Figure 1. Tectonic, atmospheric and ocean chemical changes over the past 400 Myr** | **a**, Continental distribution<sup>11</sup> with continental landmasses shown in pink, present-day coastlines in black, and the tropics ( $\pm 20^\circ$  of the equator) in beige; **b**, atmospheric  $\text{CO}_2$  concentration (multi-proxy, black line)<sup>12</sup>, and phytane-based estimates in red<sup>13</sup>; continental ice latitude<sup>5</sup> is shown as the blue line (blue shaded regions denote glaciations); **c**, continental arc length<sup>14</sup>; **d**, seafloor production rates (Methods); **e**, suture zone lengths<sup>5</sup>; **f**, fragmentation index (i.e., continental perimeter/area, as black line), and total area of continents in the tropics (red line); **g**,  $(^{87}\text{Sr}/^{86}\text{Sr})_{\text{sw}}$  from marine carbonates<sup>15</sup>, calculated as a  $\pm 0.25$  Myr window in red; **h**, normalised  $(^{87}\text{Sr}/^{86}\text{Sr})_{\text{sw}}$  curve removing the signal caused by radioactive  $^{87}\text{Rb}$  decay in the crust<sup>16</sup>.

51 moving average using a  $\pm 0.25$  Myr window (Fig. 1g). Given the  
 52 large contrast in  $^{87}\text{Sr}/^{86}\text{Sr}$  between radiogenic continents and  
 53 unradiogenic oceanic crust<sup>21</sup>,  $(^{87}\text{Sr}/^{86}\text{Sr})_{\text{sw}}$  is thought to repre-  
 54 sent a globally integrated balance in weathering flux from conti-  
 55 nental surfaces and the seafloor<sup>15,21,22</sup>. We tested this assertion  
 56 by constructing a network to explore the relationship between  
 57  $(^{87}\text{Sr}/^{86}\text{Sr})_{\text{sw}}$  and partial pressure of atmospheric carbon dioxide  
 58 ( $p\text{CO}_2$ ) since 400 Ma<sup>12</sup>. This analysis reveals a clear relation-  
 59 ship between  $(^{87}\text{Sr}/^{86}\text{Sr})_{\text{sw}}$  and  $p\text{CO}_2$  (empirical correlation =  
 60 0.57) at lag 0, which decreases with increasing lags (Extended  
 61 Data Fig. 1), confirming that they are coupled<sup>4</sup>. However, as  
 62 there are clearly secondary controls on  $(^{87}\text{Sr}/^{86}\text{Sr})_{\text{sw}}$ , and some  
 63 uncertainty in the  $\text{CO}_2$  record used<sup>12</sup>, the relationship is not  
 64 straightforward; this is a key justification for analysing what  
 65 drives these variations through time. We present our results in  
 66 terms of  $(^{87}\text{Sr}/^{86}\text{Sr})_{\text{sw}}$ —the standard framework—but also test  
 67 the sensitivity of our model to radioactive decay of  $^{87}\text{Rb}$  (to  
 68  $^{87}\text{Sr}$ ) in the crust through time<sup>16</sup>.

## 69 Building an Earth network

70 Despite progress in linking variations in  $(^{87}\text{Sr}/^{86}\text{Sr})_{\text{sw}}$  to geo-  
 71 dynamic and paleogeographic factors<sup>23</sup>, it is unclear how pro-  
 72 cesses combine to drive  $(^{87}\text{Sr}/^{86}\text{Sr})_{\text{sw}}$  variations. We con-  
 73 structed the network (Methods) with nodes for  $(^{87}\text{Sr}/^{86}\text{Sr})_{\text{sw}}$   
 74 and twelve predictor variables (Supplementary Data File S1),  
 75 with lags from 0 to 50 Myr. We present three correlation mea-  
 76 sures that summarise the relationships between the variables  
 77 and  $(^{87}\text{Sr}/^{86}\text{Sr})_{\text{sw}}$  (Figs. 2–3). First, the empirical rank (or Pear-  
 78 son product-moment) correlation ( $C_{\text{Emp}}$ ) measures the linear rela-  
 79 tionship between two variables. Although informative, this  
 80 does not account for autocorrelation, or the joint influence of  
 81 other variables. Second, the BN rank correlation ( $C_{\text{BN}}$ ) is the  
 82 modelled representation of the empirical rank correlation. In an  
 83 ideal case (i.e., a perfect model fit) this would be equal to  $C_{\text{Emp}}$ .  
 84 Third, the conditional rank correlation ( $C_{\text{Cond}}$ ) is the correlation  
 85 between two variables conditional on any other parent variables  
 86 (accounting for the effect of all nodes at shorter lags, and higher,  
 87 up in the network hierarchy; Methods).

88 We construct our network by starting with the variable with<sup>104</sup>  
 89 the highest empirical correlation (at lag 0), and systematically<sup>105</sup>  
 90 search the set of predictor variables to find maximum values of<sup>106</sup>  
 91  $C_{\text{Cond}}$  at increasing lags, up to 50 Myr (Methods). A variable<sup>107</sup>  
 92 is added to the network if its conditional correlation exceeds<sup>108</sup>  
 93 a confidence interval threshold (dependent on the number of<sup>109</sup>  
 94 original data points). The conditional correlation removes the<sup>110</sup>  
 95 influence of variables higher in the network hierarchy (and at<sup>111</sup>  
 96 earlier lags), and provides a measure of the additional infor-<sup>112</sup>  
 97 mation each subsequent lagged variable provides in explaining<sup>113</sup>  
 98  $(^{87}\text{Sr}/^{86}\text{Sr})_{\text{sw}}$  variation (Fig. 3; Extended Data Fig. 2). This ap-<sup>114</sup>  
 99 proach is based on the method for partial autocorrelation, and<sup>115</sup>  
 100 efficiently accounts for multiple joint dependencies and lags<sup>116</sup>  
 101 (Methods). Whilst our focus below is on  $C_{\text{Cond}}$ , for context<sup>117</sup>  
 102 we also provide  $C_{\text{Emp}}$  and  $C_{\text{BN}}$  (Fig. 3).<sup>118</sup>

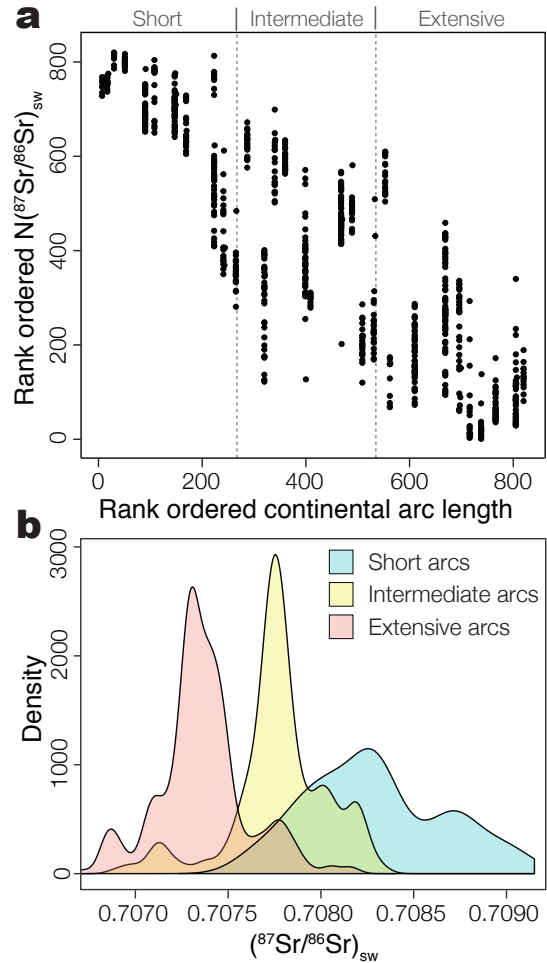


**Figure 2. Effects of continental arc extent on the strontium isotopic composition of seawater** | a, Ranked ordered normalised  $(^{87}\text{Sr}/^{86}\text{Sr})_{\text{sw}}$ <sup>16</sup> versus ranked continental arc length (see Extended Data Fig. 3 for the non-normalised and unranked versions). Note that the smallest value that occurs in the data set is ranked 1. b, Probability density for continental arc length<sup>14</sup>, identifying short (<16,100 km), intermediate (16,100–29,300 km), and extensive ( $\geq 29,300$  km) arcs (note: these divisions denote approximately equal quantiles); the distributions show that extensive continental arc systems favour low  $(^{87}\text{Sr}/^{86}\text{Sr})_{\text{sw}}$ , and vice versa.

## Identification of chemical weathering drivers

We find that the spatial extent of continental volcanic arcs<sup>14</sup> (Fig. 1c), where oceanic lithosphere is subducted beneath continental lithosphere<sup>7</sup>, is most strongly correlated with  $(^{87}\text{Sr}/^{86}\text{Sr})_{\text{sw}}$  ( $C_{\text{Emp}} = -0.79$ ;  $C_{\text{Cond}} = -0.7$ ; Figs. 2, 3a), increasing when we correct for crustal radioactive decay of  $^{87}\text{Rb}$  (ref.<sup>16</sup>;  $C_{\text{Emp}} = -0.82$ ; Fig. 2a; Extended Data Table 2). This strong relationship (Fig. 2) suggests that periods of increased continental arc volcanism have favoured unradiogenic seawater compositions, and vice versa. Today, the global continental arc system is  $\sim 14,000$  km long<sup>14</sup>, and includes regions such as the Alaska Peninsula, the Cascades and the Andean Volcanic Belt (Extended Data Fig. 4). The global arc system was three times longer ( $\sim 37,500$  km) during the Mesozoic (Fig. 1c), reflecting a sharp increase in seafloor production (Figs. 1c–d). The ocean chemical response to changing arc extent is rapid, peaking in

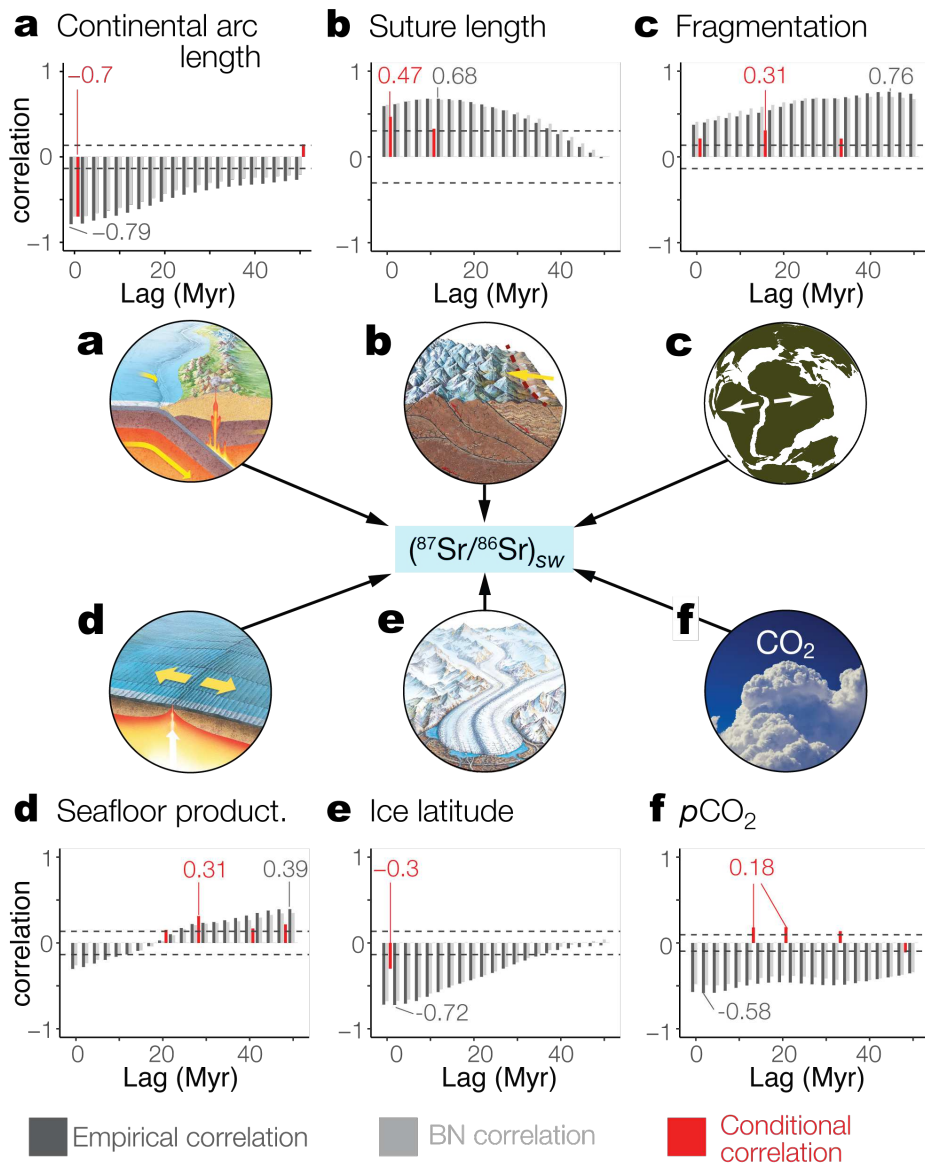


**Figure 3. Simplified network structure showing key geological processes and correlations with seawater Sr** | Graphical representation of our network, showing how the six dominant variables (a–f) influence  $(^{87}\text{Sr}/^{86}\text{Sr})_{\text{sw}}$  (Extended Data Fig. 2). The plots summarise the relationships between the relevant variable and  $(^{87}\text{Sr}/^{86}\text{Sr})_{\text{sw}}$  for all time steps in our analysis ( $n = 360$ ). The plots show  $C_{\text{Emp}}$ ,  $C_{\text{BN}}$ , and  $C_{\text{Cond}}$ , at time lags from 0 to 50 Myr in 2.5 Myr intervals. A lag of 0 means the relevant process is occurring within the same 1 Myr time-step. The values shown in gray on the plots are the highest value of  $C_{\text{Emp}}$ ; if each process were considered in isolation this value would represent the dominant time lag. However due to autocorrelation and joint dependence, the dominant processes and time lags can be better identified by peak  $C_{\text{Cond}}$  (red). The horizontal dashed lines denote 99% confidence intervals.

119 <0.5 Myr (Fig. 3a). Before exploring the importance of these<sup>176</sup>  
120 observations, we need to quantitatively evaluate how other pro-<sup>177</sup>  
121 cesses combine to drive  $(^{87}\text{Sr}/^{86}\text{Sr})_{\text{sw}}$ .<sup>178</sup>

122 Terrestrial weathering fluxes are highly sensitive to crustal<sup>179</sup>  
123 deformation<sup>1,4,8,9,10</sup>. It has been suggested that arc-continent<sup>180</sup>  
124 collisions in the tropics led to enhanced weathering of ophi-<sup>181</sup>  
125 olites and CO<sub>2</sub> drawdown, driving Phanerozoic glaciations<sup>5,182</sup>.  
126 Weathering of ultramafic lithologies on this scale should reduce<sup>183</sup>  
127  $(^{87}\text{Sr}/^{86}\text{Sr})_{\text{sw}}$ , reflecting unradiogenic inputs to oceans. To eval-<sup>184</sup>  
128 uate this, we incorporate existing suture length data<sup>5</sup> into our<sup>185</sup>  
129 network (Fig. 1e; Extended Data Fig. 5). The empirical cor-<sup>186</sup>  
130 relation between active suture length and  $(^{87}\text{Sr}/^{86}\text{Sr})_{\text{sw}}$  appears<sup>187</sup>  
131 high. However, accounting for other dominant processes (i.e.,<sup>188</sup>  
132 continental arc length), this reduces, leaving a peak  $C_{\text{Cond}} =$ <sup>189</sup>  
133 0.47 at lag 0 (Fig. 3b). The consistently positive correlations<sup>190</sup>  
134 between suture length and  $(^{87}\text{Sr}/^{86}\text{Sr})_{\text{sw}}$  (Fig. 3b) suggest that<sup>191</sup>  
135 arc-continent collisions may promote enhanced weathering of<sup>192</sup>  
136 radiogenic continental material via orogenesis and erosion<sup>4,10,193</sup>.  
137 However, it is also feasible that ophiolites acquire radiogenic<sup>194</sup>  
138 signatures during regional metamorphism<sup>24</sup>. Irrespective of the<sup>195</sup>  
139 mechanism, our analysis confirms a key role for arc-continent<sup>196</sup>  
140 collisions in driving increased weathering fluxes<sup>5</sup>.<sup>197</sup>

141 Chemical weathering is also sensitive to continental frag-<sup>198</sup>  
142 mentation, which increases the reach of oceanic moisture into<sup>199</sup>  
143 continental interiors<sup>6</sup>, but the timescales and impacts are highly<sup>200</sup>  
144 uncertain. To address this, we consider geospatial attributes of<sup>201</sup>  
145 continents through time (Methods). Using the footprint defined<sup>202</sup>  
146 by continent-ocean boundaries<sup>11</sup>, we computed the continen-<sup>203</sup>  
147 tal perimeter/area ratio<sup>25,26</sup>—a quantitative measure of crustal<sup>204</sup>  
148 fragmentation (Fig. 1f). We find the correlation between conti-<sup>205</sup>  
149 nental fragmentation and  $(^{87}\text{Sr}/^{86}\text{Sr})_{\text{sw}}$  is moderate to low (max-<sup>206</sup>  
150 imum  $C_{\text{Cond}} = 0.31$ ), and positive, consistent with enhanced<sup>207</sup>  
151 weathering of radiogenic crust during plate tectonic fragmen-<sup>208</sup>  
152 tation. The peak  $C_{\text{Cond}}$  at time lags of ~12.5–15 Myr (Fig. 3c)<sup>209</sup>  
153 is commensurate with typical timescales of rift-to-drift tran-<sup>210</sup>  
154 sitions and delayed basin connectivity following continental<sup>211</sup>  
155 breakup<sup>27</sup>. Accounting for lags of this order will be crucial to<sup>212</sup>  
156 correctly interpret associations between tectonic fragmentation<sup>213</sup>  
157 and marine biodiversity<sup>28</sup>.<sup>214</sup>

158 High temperatures and precipitation usually favour high  
159 weathering rates in tropical regions<sup>5,6</sup>. It has thus been hypoth-<sup>215</sup>  
160 esised that a high proportion of continental landmasses within  
161 the tropics could strongly influence global weathering<sup>6</sup>. We test<sup>216</sup>  
162 this by quantifying continental area within the tropical latitudi-<sup>217</sup>  
163 nal bands ( $\pm 20^\circ$  and  $\pm 10^\circ$  of the equator) at 1 Myr intervals<sup>218</sup>  
164 (Fig. 1f; Extended Data Fig. 6), and integrate this in our net-<sup>219</sup>  
165 work. The land surface area within the tropics has increased<sup>220</sup>  
166 over 400–0 Ma (Fig. 1f), but makes a negligible contribution to<sup>221</sup>  
167 weathering fluxes from the continental surface (Extended Data<sup>222</sup>  
168 Fig. 2). This could be due to development of deep, indurated<sup>223</sup>  
169 soil profiles in tropical drainage basins that lead to very low<sup>224</sup>  
170 (transport-limited) weathering intensity<sup>29</sup>. Similarly, the spa-<sup>225</sup>  
171 tial extent of LIPs through time<sup>20</sup> is only very weakly related<sup>226</sup>  
172 to  $(^{87}\text{Sr}/^{86}\text{Sr})_{\text{sw}}$  (Extended Data Fig. 2), possibly because they<sup>227</sup>  
173 are typically flat lying rather than mountainous terrains. This<sup>228</sup>  
174 suggests that environmental perturbations associated with LIPs<sup>229</sup>  
175 are most likely due to changes in volcanic CO<sub>2</sub> fluxes<sup>30</sup> rather<sup>230</sup>

than enhanced weathering of mafic lithologies.

It is well established that seafloor basalt alteration<sup>31</sup> and  
hydrothermal venting decrease  $(^{87}\text{Sr}/^{86}\text{Sr})_{\text{sw}}$  (i.e. toward mid-  
ocean ridge basalt [MORB] mantle  $^{87}\text{Sr}/^{86}\text{Sr} \approx 0.7035$ ; ref.<sup>22</sup>).  
Therefore,  $(^{87}\text{Sr}/^{86}\text{Sr})_{\text{sw}}$  is expected to scale inversely with  
seafloor production rate (Fig. 1d), which we calculate as the  
product of ridge length and spreading rate (Extended Data Fig.  
7), adapting an existing plate model<sup>26</sup>. We find that seafloor  
productivity is negatively correlated with  $(^{87}\text{Sr}/^{86}\text{Sr})_{\text{sw}}$  at short  
lags (Fig. 3d), reflecting the effects of early high temperature  
alteration of basalts along ridge axes<sup>32</sup>. The seafloor weath-  
ering contribution becomes negligible ~15–20 Myr after em-  
placement, suggesting that seafloor is not weathered apprecia-  
bly after this time. This is strikingly consistent with hydrother-  
mal models<sup>33</sup> and observations of secondary minerals in ocean  
crust<sup>35,34</sup>, which indicate that ~70–80% of fluid flux occurs in  
seafloor within 20 Myr of formation. We find that radiogenic  
continental weathering sources dominate the  $(^{87}\text{Sr}/^{86}\text{Sr})_{\text{sw}}$  sig-  
nal at lags >20 Myr, explaining the switch to a positive correla-  
tion (Fig. 3d).

Glacial intensity is also known to influence  $(^{87}\text{Sr}/^{86}\text{Sr})_{\text{sw}}$ <sup>36</sup>.  
Investigating the effect of continental ice coverage, we find a  
strong empirical correlation between latitudinal extent of ice  
sheets (Fig. 1b) (as a proxy for the severity of glaciation and  
global climate<sup>5</sup>) and  $(^{87}\text{Sr}/^{86}\text{Sr})_{\text{sw}}$  (-0.72; Fig. 3e; Extended  
Data Fig. 8), supporting the notion that glaciations cause in-  
tensified weathering of continental crust<sup>21,36,37,38</sup>. This is likely  
due to preferential weathering of radiogenic minerals like bi-  
otite in comminuted rock flour characteristic of glaciated catch-  
ments<sup>37,38</sup>. The conditional correlation is low due to collinear-  
ity between ice extent, and arc and suture lengths. Observa-  
tions suggest weathering influences atmospheric CO<sub>2</sub> concen-  
tration<sup>12</sup> (Fig. 1f; Extended Data Fig. 1), but also provide evi-  
dence for a feedback whereby CO<sub>2</sub> influences weathering (neg-  
ative  $C_{\text{Emp}} = -0.58$  where  $(^{87}\text{Sr}/^{86}\text{Sr})_{\text{sw}}$  lags CO<sub>2</sub> by 0.5–2.5  
Myr). A weak, but statistically significant positive  $C_{\text{Cond}}$  be-  
tween CO<sub>2</sub> and  $(^{87}\text{Sr}/^{86}\text{Sr})_{\text{sw}}$  at lags >10 Myr (Fig. 3f) suggests  
a weak negative carbonate-silicate feedback operating over tens  
of millions of years. This appears to be a secondary effect.

### Central role for volcanic arc weathering

Our analysis indicates that continental volcanic arc extent ex-  
erts the strongest influence on  $(^{87}\text{Sr}/^{86}\text{Sr})_{\text{sw}}$  as a proxy for global  
chemical weathering, consistent with regional studies<sup>39,40</sup>, and  
with the observation that chemical weathering of island arcs  
dominates the oceanic Sr budget today<sup>41</sup>. Continental arcs are  
an important contributor to the atmospheric CO<sub>2</sub> inventory, ow-  
ing to a propensity for decarbonation reactions in the conti-  
nental lithosphere<sup>7</sup>. The strongly negative correlation between  
continental arc length and  $(^{87}\text{Sr}/^{86}\text{Sr})_{\text{sw}}$  (Figs. 2 and 3a) is con-  
sistent with the hypothesis that their formation and spatial ex-  
tent governs icehouse-greenhouse transitions<sup>7</sup>.

The high CO<sub>2</sub> outgassing flux and greenhouse conditions  
associated with extensive continental arcs<sup>7</sup> favour intensified  
chemical weathering<sup>1,8,9</sup>. Today, continental volcanic arcs are  
among the highest topographic—and fastest eroding—surface

231 features on Earth<sup>39</sup>, supplying Ca-Mg silicates to the ocean<sup>285</sup>  
232 over tens of millions of years<sup>40</sup>. Hydrothermal activity max-<sup>286</sup>  
233 imises water-rock interactions, which, given the enhanced oro-<sup>287</sup>  
234 graphic precipitation typical in these regions, results in extreme<sup>288</sup>  
235 chemical denudation rates<sup>42,43</sup>. For example, the present-day<sup>289</sup>  
236 Andes (Extended Data Fig. 4) dominates dissolved ion fluxes<sup>290</sup>  
237 to the Amazon River<sup>44</sup>, fuelling Earth's greatest offshore river<sup>291</sup>  
238 plume. Today, continental arcs are predominantly unradiogenic<sup>292</sup>  
239 (Extended Data Fig. 4), with mean  $^{87}\text{Sr}/^{86}\text{Sr}$  values of 0.7044<sup>293</sup>  
240 (N = 5498; median = 0.704, mode = 0.7035), only slightly<sup>294</sup>  
241 higher than typical MORB and ocean island basalts<sup>45</sup>. Thus,<sup>295</sup>  
242 prolonged cycles of arc assembly, erosion and weathering<sup>39,40</sup><sup>296</sup>  
243 likely drove seawater toward the unradiogenic compositions we<sup>297</sup>  
244 observe (Figs. 2–3). Greenhouse conditions linked to extensive<sup>298</sup>  
245 arcs<sup>7</sup> should promote increased bottom water temperatures and<sup>299</sup>  
246 enhanced seafloor weathering<sup>46</sup>, further reducing  $(^{87}\text{Sr}/^{86}\text{Sr})_{\text{sw}}$ <sup>300</sup>

247 Continental volcanic arcs are predisposed to acid-  
248 intermediate magmatism, favouring zircon production<sup>47</sup>.  
249 The interpretation that continental arcs drive global chemical  
250 weathering fluxes (Fig. 2) is therefore consistent with an  
251 observed increase in detrital zircon abundance during green-  
252 house intervals<sup>7</sup>. The latter implicates increased transport and  
253 weathering of arc detritus to ocean basins when continental  
254 arcs are longest. Our analysis confirms that the  $^{87}\text{Sr}/^{86}\text{Sr}$   
255 of zircon-bearing igneous rocks strongly correlates with  
256  $(^{87}\text{Sr}/^{86}\text{Sr})_{\text{sw}}$  over the past 400 Myr (Extended Data Table 2),  
257 suggesting global chemical weathering is tightly coupled to the  
258 composition of continental igneous lithologies<sup>16</sup>. The correla-  
259 tion between igneous  $^{87}\text{Sr}/^{86}\text{Sr}$  and  $(^{87}\text{Sr}/^{86}\text{Sr})_{\text{sw}}$  is highest<sup>16</sup>  
260 when arc systems are longest<sup>14</sup>. It is therefore probable that  
261 the spatial extent of continental arcs drives  $(^{87}\text{Sr}/^{86}\text{Sr})_{\text{sw}}$  via the  
262 proportional availability of weatherable igneous catchments.  
263 This finding draws specific attention to the types of rock and  
264 climate conditions that offer the best potential for accelerated  
265 CO<sub>2</sub> drawdown in enhanced weathering schemes designed to  
266 counteract current global climate change<sup>48</sup>.

## 267 Summary

268 We have developed a new data mining approach based on  
269 conditional probability estimation, to disentangle complex in-  
270 terdependencies between solid Earth, hydrosphere, and atmo-  
271 spheric processes, over the past 400 million years. This ap-  
272 proach has significant potential to aid interpretation of complex  
273 Earth data exhibiting high dimensional dependency on different  
274 spatial and temporal scales.

275 It is widely accepted that continental arcs modulate atmo-  
276 spheric CO<sub>2</sub> levels<sup>7,49</sup> and represent a major agent of crustal  
277 growth through post-Archean Earth history via arc accretion  
278 processes<sup>39</sup>. Our analysis indicates that arcs have also domi-  
279 nated global chemical weathering fluxes, which determine the  
280 Sr isotopic composition of seawater,  $(^{87}\text{Sr}/^{86}\text{Sr})_{\text{sw}}$ , over the past  
281 400 Myr. This revises conventional concepts that  $(^{87}\text{Sr}/^{86}\text{Sr})_{\text{sw}}$   
282 is driven by competition between weathering of the seafloor  
283 and continental interiors. Arc weathering causes reduction in  
284  $(^{87}\text{Sr}/^{86}\text{Sr})_{\text{sw}}$  while continental weathering causes increase in

$(^{87}\text{Sr}/^{86}\text{Sr})_{\text{sw}}$ . Thus, our findings of arc dominance in weather-  
ing help explain enigmatic low  $(^{87}\text{Sr}/^{86}\text{Sr})_{\text{sw}}$  during greenhouse  
climates, where the higher temperatures should according to  
conventional concepts have promoted greater continental crust  
weathering<sup>8</sup>, driving increased  $(^{87}\text{Sr}/^{86}\text{Sr})_{\text{sw}}$ .

Our results indicate that continental arcs provide a self-  
regulating thermostat, gradually removing atmospheric CO<sub>2</sub> via  
rock weathering reactions that offset their more rapid high vol-  
canic CO<sub>2</sub> outgassing fluxes. Conversely, when continental arc  
extent reduces, global CO<sub>2</sub> emissions decrease, arc weather-  
ing slows down, and continental ice sheets become the prin-  
cipal agent of physical and chemical weathering, driving in-  
creased  $(^{87}\text{Sr}/^{86}\text{Sr})_{\text{sw}}$ . Through this regulation of atmospheric  
CO<sub>2</sub> levels over geological timescales, continental volcanic arcs  
played a central role in maintaining habitability over the course  
of Earth history even in the face of dramatic external drivers.

## Online content

Any methods, additional references, Nature Research re-  
porting summaries, source data, extended data, supplement-  
ary information, acknowledgements, peer review informa-  
tion; details of author contributions and competing interests;  
and statements of data and code availability are available at  
<https://doi.org/10.1038/s12345-111-2222-3>.

## References

1. L. R. Kump, S. L. Brantley, and M. A. Arthur. Chemical weathering, atmospheric CO<sub>2</sub>, and climate. *Annual Review of Earth and Planetary Sciences*, 28(1):611–667, 2000.
2. J. F. Kasting. The Goldilocks planet? How silicate weathering maintains Earth “just right”. *Elements*, 15(4):235–240, 2019.
3. D. E. Penman, J. K. Caves Rügenstein, D. E. Ibarra, and M. J. Winnick. Silicate weathering as a feedback and forcing in Earth's climate and carbon cycle. *Earth-Science Reviews*, 209:103298, 2020.
4. M. E. Raymo and W. F. Ruddiman. Tectonic forcing of late Cenozoic climate. *Nature*, 359(6391):117–122, 1992.
5. F. A. Macdonald, N. L. Swanson-Hysell, Y. Park, L. Lisiecki, and O. Jagoutz. Arc-continent collisions in the tropics set Earth's climate state. *Science*, 364(6436):181–184, 2019.
6. Y. Donnadieu, Y. Goddérís, G. Ramstein, A. Nédélec, and J. Meert. A ‘snowball Earth’ climate triggered by continental break-up through changes in runoff. *Nature*, 428(6980):303–306, 2004.
7. N. R. McKenzie, B. K. Horton, S. E. Loomis, D. F. Stockli, N. J. Planavsky, and C.-T. A. Lee. Continental arc volcanism as the principal driver of icehouse-greenhouse variability. *Science*, 352(6284):444, 2016.
8. J. C. G. Walker, P. B. Hays, and J. F. Kasting. A negative feedback mechanism for the long-term stabilization of Earth's surface temperature. *Journal of Geophysical Research: Oceans*, 86(C10):9776–9782, 1981.
9. R. A. Berner and E. K. Berner. Silicate weathering and climate. In William F. Ruddiman, editor, *Tectonic Uplift and Climate Change*, pages 353–365. Springer US, Boston, MA, 1997.
10. J. M. Edmond. Himalayan tectonics, weathering processes, and the strontium isotope record in marine limestones. *Science*, 258(5088):1594, 1992.
11. K. J. Matthews, K. T. Maloney, S. Zahirovic, S. E. Williams, M. Seton, and R. D. Müller. Global plate boundary evolution and kinematics since the late Paleozoic. *Global and Planetary Change*, 146:226–250, 2016.
12. G. L. Foster, D. L. Royer, and D. J. Lunt. Future climate forcing potentially without precedent in the last 420 million years. *Nature Communications*, 8:14845, 2017.

13. C. R. Witkowski, J. W. H. Weijers, B. Blais, S. Schouten, and J. S. Sinninghe Damsté. Molecular fossils from phytoplankton reveal secular  $PCO_2$  trend over the Phanerozoic. *Science Advances*, 4(11):eaat4556, 2018.
14. W. Cao, C.-T. A. Lee, and J. S. Lackey. Episodic nature of continental arc activity since 750 Ma: A global compilation. *Earth and Planetary Science Letters*, 461:85–95, 2017.
15. J. Veizer, D. Ala, K. Azmy, P. Bruckschen, D. Buhl, F. Bruhn, G. A. F. Carden, A. Diener, S. Ebner, Y. Godderis, T. Jasper, C. Korte, F. Pawellek, O. G. Podlaha, and H. Strauss.  $^{87}Sr/^{86}Sr$ ,  $\delta^{13}C$  and  $\delta^{18}O$  evolution of Phanerozoic seawater. *Chemical Geology*, 161(1):59–88, 1999.
16. C. P. Bataille, A. Willis, X. Yang, and X.-M. Liu. Continental igneous rock composition: A major control of past global chemical weathering. *Science Advances*, 3(3):e1602183, 2017.
17. T. Hincks, W. Aspinall, R. Cooke, and T. Gernon. Oklahoma’s induced seismicity strongly linked to wastewater injection depth. *Science*, 359(6381):1251, 2018.
18. J. L. Morris, M. N. Puttick, J. W. Clark, D. Edwards, P. Kenrick, S. Presnel, C. H. Wellman, Z. Yang, H. Schneider, and P. C. J. Donoghue. The timescale of early land plant evolution. *Proceedings of the National Academy of Sciences*, 115(10):E2274, 2018.
19. R. D. Müller, J. Cannon, X. Qin, R. J. Watson, M. Gurnis, S. Williams, T. Pfaffelmoser, M. Seton, S. H. J. Russell, and S. Zahirovic. GPlates: Building a virtual Earth through deep time. *Geochemistry, Geophysics, Geosystems*, 19(7):2243–2261, 2018.
20. L. Johansson, S. Zahirovic, and R. D. Müller. The interplay between the eruption and weathering of large igneous provinces and the deep-time carbon cycle. *Geophysical Research Letters*, 45(11):5380–5389, 2018.
21. B. Peucker-Ehrenbrink and G. J. Fiske. A continental perspective of the seawater  $^{87}Sr/^{86}Sr$  record: A review. *Chemical Geology*, 510:140–165, 2019.
22. H. Elderfield and A. Schultz. Mid-ocean ridge hydrothermal fluxes and the chemical composition of the ocean. *Annual Review of Earth and Planetary Sciences*, 24(1):191–224, 1996.
23. C. Vérard, C. Hochard, P. O. Baumgartner, G. M. Stampfli, and M. Liu. Geodynamic evolution of the Earth over the Phanerozoic: Plate tectonic activity and palaeoclimatic indicators. *Journal of Palaeogeography*, 4(2):167–188, 2015.
24. A. M. Stueber. Abundances of K, Rb, Sr and Sr isotopes in ultramafic rocks and minerals from western North Carolina. *Geochimica et Cosmochimica Acta*, 33(5):543–553, 1969.
25. J.-P. Cogné and E. Humler. Global scale patterns of continental fragmentation: Wilson’s cycles as a constraint for long-term sea-level changes. *Earth and Planetary Science Letters*, 273(3):251–259, 2008.
26. A. S. Meredith, S. E. Williams, S. Brune, A. S. Collins, and R. D. Müller. Rift and plate boundary evolution across two supercontinent cycles. *Global and Planetary Change*, 173:1–14, 2019.
27. R. Granot and J. Dymant. The Cretaceous opening of the South Atlantic Ocean. *Earth and Planetary Science Letters*, 414:156–163, 2015.
28. J.-x. Fan, S.-z. Shen, D. H. Erwin, P. M. Sadler, N. MacLeod, Q.-m. Cheng, X.-d. Hou, J. Yang, X.-d. Wang, Y. Wang, H. Zhang, X. Chen, G.-x. Li, Y.-c. Zhang, Y.-k. Shi, D.-x. Yuan, Q. Chen, L.-n. Zhang, C. Li, and Y.-y. Zhao. A high-resolution summary of Cambrian to Early Triassic marine invertebrate biodiversity. *Science*, 367(6475):272, 2020.
29. J. Hartmann, N. Moosdorf, R. Lauerwald, M. Hinderer, and A. J. West. Global chemical weathering and associated P-release —The role of lithology, temperature and soil properties. *Chemical Geology*, 363:145–163, 2014.
30. N. R. McKenzie and H. Jiang. Earth’s outgassing and climatic transitions: The slow burn towards environmental “catastrophes”? *Elements*, 15:325–330, 2019.
31. S. R. Hart, A. J. Erlank, and E. J. D. Kable. Sea floor basalt alteration: Some chemical and Sr isotopic effects. *Contributions to Mineralogy and Petrology*, 44(3):219–230, 1974.
32. M. J. Mottl and C. G. Wheat. Hydrothermal circulation through mid-ocean ridge flanks: Fluxes of heat and magnesium. *Geochimica et Cosmochimica Acta*, 58(10):2225–2237, 1994.
33. R. D. Müller, A. Dutkiewicz, M. Seton, and C. Gaina. Seawater chemistry driven by supercontinent assembly, breakup, and dispersal. *Geology*, 41(8):907–910, 2013.
34. E. Booi, W. E. Gallahan, and H. Staudigel. Ion-exchange experiments and Rb/Sr dating on celadonites from the Troodos ophiolite, Cyprus. *Chemical Geology*, 126(2):155–167, 1995.
35. R. M. Coggon, D. A. H. Teagle, C. E. Smith-Duque, J. C. Alt, and M. J. Cooper. Reconstructing past seawater Mg/Ca and Sr/Ca from mid-ocean ridge flank calcium carbonate veins. *Science*, 327(5969):1114, 2010.
36. J. D. Blum and Y. Erel. A silicate weathering mechanism linking increases in marine  $^{87}Sr/^{86}Sr$  with global glaciation. *Nature*, 373(6513):415–418, 1995.
37. S. Prestrud Anderson, J. I. Drever, and N. F. Humphrey. Chemical weathering in glacial environments. *Geology*, 25(5):399–402, 1997.
38. D. Vance, D. A. H. Teagle, and G. L. Foster. Variable Quaternary chemical weathering fluxes and imbalances in marine geochemical budgets. *Nature*, 458(7237):493–496, 2009.
39. C.-T. A. Lee, S. Thurner, S. Paterson, and W. Cao. The rise and fall of continental arcs: Interplays between magmatism, uplift, weathering, and climate. *Earth and Planetary Science Letters*, 425:105–119, 2015.
40. H. Jiang and C.-T. A. Lee. On the role of chemical weathering of continental arcs in long-term climate regulation: A case study of the Peninsular Ranges batholith, California (USA). *Earth and Planetary Science Letters*, 525:115733, 2019.
41. C. J. Allègre, P. Louvat, J. Gaillardet, L. Meynadier, S. Rad, and F. Capmas. The fundamental role of island arc weathering in the oceanic Sr isotope budget. *Earth and Planetary Science Letters*, 292(1):51–56, 2010.
42. A. J. West, A. Galy, and M. Bickle. Tectonic and climatic controls on silicate weathering. *Earth and Planetary Science Letters*, 235(1):211–228, 2005.
43. J. Gaillardet, P. Louvat, and E. Lajeunesse. Rivers from volcanic island arcs: The subduction weathering factory. *Applied Geochemistry*, 26:S350–S353, 2011.
44. M. E. McClain and R. J. Naiman. Andean influences on the biogeochemistry and ecology of the Amazon River. *BioScience*, 58(4):325–338, 2008.
45. R. K. O’Nions, P. J. Hamilton, and N. M. Evensen. Variations in  $^{143}Nd/^{144}Nd$  and  $^{87}Sr/^{86}Sr$  ratios in oceanic basalts. *Earth and Planetary Science Letters*, 34(1):13–22, 1977.
46. O. V. Brady and S. R. Gislason. Seafloor weathering controls on atmospheric  $CO_2$  and global climate. *Geochimica et Cosmochimica Acta*, 61(5):965–973, 1997.
47. C.-T. A. Lee and O. Bachmann. How important is the role of crystal fractionation in making intermediate magmas? Insights from Zr and P systematics. *Earth and Planetary Science Letters*, 393:266–274, 2014.
48. D. J. Beerling, E. P. Kantzas, M. R. Lomas, P. Wade, R. M. Eufrazio, P. Renforth, B. Sarkar, M. G. Andrews, R. H. James, C. R. Pearce, J.-F. Mercure, H. Pollitt, P. B. Holden, N. R. Edwards, M. Khanna, L. Koh, S. Quegan, N. F. Pidgeon, I. A. Janssens, J. Hansen, and S. A. Banwart. Potential for large-scale  $CO_2$  removal via enhanced rock weathering with croplands. *Nature*, 583(7815):242–248, 2020.
49. E. Mason, M. Edmonds, and A. V. Turczyn. Remobilization of crustal carbon may dominate volcanic arc emissions. *Science*, 357(6348):290–294, 2017.

**Publisher’s note:**

Springer Nature remains neutral with regard to jurisdictional claims in published maps and institutional affiliations.

© The Author(s), under exclusive licence to Springer Nature Limited 2020

## 301 Methods 355

### 302 1.0. Bayesian Network analysis 357

303 Here we outline the methodology for our Bayesian Network<sup>358</sup>  
304 (BN) analysis. We use the UNINET COM library<sup>50</sup> in Visual Stu-<sup>359</sup>  
305 dio (C++)<sup>51</sup> to perform data mining on the time-series detailed<sup>360</sup>  
306 in section 2.0 (below). The approach enables the identification<sup>361</sup>  
307 of dominant correlations for a range of geophysical and geo-<sup>362</sup>  
308 chemical variables with the strontium isotope ratio of seawater<sup>363</sup>  
309 ( $^{87}\text{Sr}/^{86}\text{Sr}$ )<sub>sw</sub> through geological time as a proxy for global<sup>364</sup>  
310 chemical weathering<sup>15,16</sup>. All initial data processing and GIS<sup>365</sup>  
311 analysis is performed in R<sup>52</sup>. 366

312 Our analysis considers data for the time period from 410 Ma<sup>367</sup>  
313 to 0 Ma, using regularised time-series with a time step of 0.5<sup>368</sup>  
314 Myr. These time-series are provided in Supplementary Data<sup>369</sup>  
315 File S1 (Fig. 1). As many of the individual time-series are based<sup>370</sup>  
316 on measurements, estimates or model values irregularly spaced<sup>371</sup>  
317 in time, we interpolate to obtain regular (0.5 Myr) time-series<sup>372</sup>  
318 to match the resolution of the CO<sub>2</sub> record used<sup>12</sup>. For cases<sup>373</sup>  
319 with multiple observations in a given time interval, a moving<sup>374</sup>  
320 average is applied (again with a 0.5 Myr window). The number<sup>375</sup>  
321 of original data points before interpolation (and accounting for<sup>376</sup>  
322 lags) is used to estimate confidence interval thresholds (CI<sub>thresh</sub>)<sup>377</sup>  
323 for rank correlation coefficients for each of the variables with<sup>378</sup>  
324 ( $^{87}\text{Sr}/^{86}\text{Sr}$ )<sub>sw</sub>. The CI (in this case the 99 percentile) threshold<sup>379</sup>  
325 determines whether or not a particular lagged variable is re-<sup>380</sup>  
326 tained in the model (described in detail in section 4.0). We also<sup>381</sup>  
327 generate multiple lagged series using average values for each<sup>382</sup>  
328 of the variables in 2.5 Myr intervals, up to 50 Myr. A lag of 0<sup>383</sup>  
329 means the processes occur within the same time step (t, Myr), a<sup>384</sup>  
330 lag of 2.5 denotes the average value from t-2.5 to t-0.5 Myr etc.<sup>385</sup>

331 It is important to note that we also repeated the BN data min-<sup>386</sup>  
332 ing using 1 Myr interval input data, and the differences in the<sup>387</sup>  
333 results were negligible. We impose CI thresholds based on the<sup>388</sup>  
334 original number of observations, not the length of the interpo-<sup>389</sup>  
335 lated time-series. 390

### 336 2.0. Network Nodes 392

337 The principal aim of our analysis is to identify the vari-<sup>393</sup>  
338 ables that are most strongly correlated with ( $^{87}\text{Sr}/^{86}\text{Sr}$ )<sub>sw</sub> (the<sup>394</sup>  
339 ‘node of interest’), and at what time lags, in order to quan-<sup>395</sup>  
340 titatively understand the primary geological processes driving<sup>396</sup>  
341 chemical weathering. We used the variation in ( $^{87}\text{Sr}/^{86}\text{Sr}$ )<sub>sw</sub><sup>397</sup>  
342 ratios derived from marine carbonates<sup>15</sup> (Fig. 1g). These raw<sup>398</sup>  
343 ( $^{87}\text{Sr}/^{86}\text{Sr}$ )<sub>sw</sub> data produce an irregular time-series with around<sup>399</sup>  
344 4,000 observations spanning 519.4 to 0 Ma, with a maximum<sup>400</sup>  
345 interval of 10.2 Myr. To generate a regular time-series for our<sup>401</sup>  
346 ‘node of interest’ we took a moving average of ( $^{87}\text{Sr}/^{86}\text{Sr}$ )<sub>sw</sub><sup>402</sup>  
347 using a rolling window of  $\pm 0.25$  Myr. We do not consider<sup>403</sup>  
348 lagged values for Sr here, as we are primarily interested in iden-<sup>404</sup>  
349 tifying the processes that lead ( $^{87}\text{Sr}/^{86}\text{Sr}$ )<sub>sw</sub>. We do however<sup>405</sup>  
350 present a separate analysis of the relationship between lagged<sup>406</sup>  
351 ( $^{87}\text{Sr}/^{86}\text{Sr}$ )<sub>sw</sub> and CO<sub>2</sub> (Extended Data Fig. 1). 407

352 The variables investigated are: 408

- 353 1. **Plate tectonic fragmentation:** Continental areas were es-<sup>410</sup>  
354 timated from shapefiles generated by the open-source plate<sup>411</sup>

tectonic reconstruction software **GPlates**<sup>19,53</sup>. We used  
the plate tectonic reconstruction of Matthews et al.<sup>11</sup> for  
extracting latitudinal and time-sensitive data for our anal-  
ysis. This plate model is a synthesis of the Domeier and  
Torsvik<sup>54</sup> model for the Late Palaeozoic and the Müller et  
al.<sup>55</sup> model for the Mesozoic and Cenozoic. All data were  
extracted with the plate model in a palaeomagnetic refer-  
ence frame, and the output comprises georeferenced maps  
of continent boundaries at 1 million year (Myr) intervals  
from 410 Ma to the present.

Areas were calculated by taking continental polygons  
(which characterise the shape and location of all the con-  
tinental landmasses) from the GPlates shapefiles<sup>11</sup>, and  
splitting them into 6 bands according to latitude (90–  
20°N, 20–10°N, 10–0°N, 0–10°S, 10–20°S, 20–90°S).  
The **R**saga package function *rsaga.intersect.polygons* is  
used to split the continental shapes by latitude, working in  
WGS84 global reference system coordinates (EPSG4326).  
The total continental area within each latitude band is cal-  
culated by first ‘dissolving’ and cleaning the polygons  
using the *rsaga.geoprocessor* function *shapes-polygons*,  
then calculating the total area using the *areaPolygon* func-  
tion from the **R** *geosphere* package. Area is calculated  
in m<sup>2</sup>, and—accounting for the accuracy of shapefiles and  
the coordinate transformation from longitude/latitude—is  
considered accurate to approximately 2 significant figures.  
This is reasonable given the model uncertainty and resolu-  
tion.

We measured the perimeter of continental landmasses  
through time using the *perimeter* function from the **R** *geo-  
sphere* package, and adapted the method of Cogné and  
Humler<sup>25</sup> and Merdith et al.<sup>26</sup> to compute the continen-  
tal perimeter/area ratio—a measure of how “fragmented”  
the continents are through time (Fig. 1f; Supplementary  
Data File S1). In contrast to ref.<sup>26</sup> we do not apply a mini-  
mum area threshold, as for the time period we are consid-  
ering, we only require the reconstructions of Matthews et  
al.<sup>11</sup> and do not need to incorporate other plate models of  
variable spatial resolution. We do however remove ‘holes’  
with areas  $< 5 \times 10^{11}$  m<sup>2</sup>, primarily to eliminate the ex-  
tremely narrow void spaces (slithers) that occur where ad-  
jacent continental polygons never fully join due to their ge-  
ometry and resolution in the model. Leaving these ‘holes’  
in place significantly inflates the perimeter estimate at cer-  
tain time steps, and they can be clearly identified as erro-  
neous gaps from inspection of the individual shape-files.  
Units of fragmentation are m<sup>-1</sup> (perimeter/area), and are  
extracted at 1 Myr intervals, then interpolated to 0.5 Myr.

- 521 2. **Land surface area within the tropics (a:  $\pm 10^\circ$ , and  
b:  $\pm 20^\circ$  of the equator):** The area of the continental land  
surface (a) within 10° degrees of the equator (i.e., the trop-  
ical rain belt<sup>5</sup>) and (b)  $\pm 20^\circ$  of the equator were measured  
as described above, again using shapefiles exported from  
**GPlates** and processed in **R**. The latitudinal distribution  
of continental landmasses (within both  $\pm 20^\circ$  (Fig. 1f) and  
 $\pm 10^\circ$  bands) and the fractional areas of continental land-  
masses in the equatorial bands (i.e., area within the belt

divided by the total crustal area) through time are shown in Extended Data Figure 6, and the data are available in Supplementary Data File S1. The result is a 1 Myr interval time-series (units:  $\text{m}^2$ ), interpolated to 0.5 Myr for the BN analysis.

**3. Seafloor production rates:** We calculated seafloor production rates as the product of ridge length and spreading rate of each discrete spreading segment (i.e., each mid-ocean ridge segment separated by a transform boundary) at 1 Myr time steps, using the **pyGPlates** python library. The data were extracted from the Matthews et al.<sup>11</sup> plate model. The spreading segments were defined by obtaining the tangent to the midpoint of the spreading segment and measuring the angle between this and the great circle of the stage pole orientation (i.e., spreading direction) that passes through the segment midpoint (Extended Data Fig. 7). If this angle exceeds  $70^\circ$ , it is assumed to represent a spreading segment, and the full spreading rate was extracted and multiplied by the length of the segment. The sum of all segments  $\times$  full spreading rate was calculated at 1 Myr intervals to give total seafloor production. Further details on this approach are provided in Extended Data Fig. 7.

A key uncertainty in the construction of seafloor production rates is that very little oceanic lithosphere older than 200 Ma is preserved today. However, our analysis does not concern time sensitive evolution of oceanic lithosphere (such that is required for understanding how oceanic volume changes through time, or the delivery of volatiles to trenches, for instance). Instead, we just require a measure of the volume of new crust formed through time. The global tectonic models used to estimate our seafloor production rates are underpinned by many geological constraints. For example, Atlantic-style oceans that opened during the Palaeozoic (e.g., the Meso- and Neotethys Oceans) are well constrained by rift-drift records and palaeomagnetic data, allowing a reasonable first-order estimate of ocean basin evolution, as implemented in plate models. The Panthalassa Ocean basin in the Matthews et al.<sup>11</sup> model was constructed by Domeier and Torsvik<sup>54</sup> to ensure that spreading rate and ridge length was sufficient to ensure convergence at all subduction zones that enclosed the ocean basin. We therefore consider that—while a non-unique solution—the evolution of this ocean basin in the Palaeozoic provides a robust minimum estimate of the volume of ocean crust added to the globe over this time. Finally, one of the implications of our analysis for the past 410 Myrs is that seafloor production rate exerts a relatively weak control on  $(^{87}\text{Sr}/^{86}\text{Sr})_{\text{sw}}$  through time. To test the sensitivity of this result to the uncertainty in spreading rates prior to 200 Ma, we developed a BN for the past 200 Myrs, when seafloor spreading rates are much better constrained. We found that the empirical correlation between seafloor production rates and  $(^{87}\text{Sr}/^{86}\text{Sr})_{\text{sw}}$  reduces even further (i.e., relative to the 410 Myr network; from -0.28 to -0.16). This test, targeting the interval with the highest certainty, provides confidence that seafloor production rate is of secondary importance in global chemical weathering

and has been particularly weak since the early Jurassic. The output is a 1 Myr interval time-series (units:  $\text{km}^2/\text{Myr}$ ), which we interpolate to 0.5 Myr for purposes of our analysis.

**4. Continental arc length:** We used a global compilation of continental volcanic arc lengths<sup>14</sup> that is based on the spatial extent of granitoids, currently exposed at the Earth's surface, associated with continental arc magmatism. Accordingly, these estimates are independent from any plate model used in our analysis. Here, the minimum length is based on the actual (i.e., observed) extent of the surface exposure of the granitoids, and the maximum length is based on the geological interpretation of the original spatial extent of the arcs (described in the Supplementary Information accompanying Cao et al.<sup>14</sup>). It must be noted that, for the present-day, these estimates omit several areas experiencing continental subduction (e.g., under Zealandia, flat slab subduction in the Andes). In most cases, the minimum and maximum lengths are equal, and in cases where these deviated we used the average length value—noting that the difference between the minimum/maximum and the average length is rather low ( $<11.5\%$ ) during the period of interest (Fig. 1c). The time-series (units: km) is regular with a 1 Myr interval, interpolated to 0.5 Myr.

**5. Suture length:** We used a database of suture zone length<sup>5</sup> that records sites of ophiolite obduction during arc-continent collisions. Here, the suture zone lengths were estimated using the observed spatial extent of ophiolites based on published geological maps and global lithological compilations. Macdonald et al.<sup>5</sup> reconstructed the locations of suture zones throughout the Phanerozoic using paleogeographic models. They estimated the duration of suture zone activity using the onset of ophiolite obduction (as evidenced by the first occurrence of arc exhumation), which they defined as the first appearance of ophiolite-derived detritus in the foreland; and the termination of foreland deposition was taken to mark the cessation of ophiolite obduction (procedure is described in the Supplementary Information accompanying ref.<sup>5</sup>). The time-series (units: km) is regular with a 5 Myr interval, interpolated to 0.5 Myr.

**6. Atmospheric  $\text{CO}_2$  concentration:** We used a compilation of the partial pressure of atmospheric carbon dioxide ( $p\text{CO}_2$ ) for the past 420 Ma derived from multi-proxy measurements ( $N=1241$ ; from the literature and covering five independent techniques; ref.<sup>12</sup>). Foster et al.<sup>12</sup> used a set of criteria to screen and standardise these records, and applied Monte Carlo resampling and a local polynomial regression (LOESS) fit to the resulting data series. We used the maximum probability  $p\text{CO}_2$  data from ref.<sup>12</sup> (Supplementary Data File S1), with associated 68 and 95 percentile ranges (Fig. 1b). We note that recent phytane-based measurements<sup>13</sup> are in reasonable agreement with this long-term  $p\text{CO}_2$  record (Fig. 1b). The time-series from Foster et al.<sup>12</sup> (units: ppm) is regular with a 0.5 Myr interval.

**7. Latitudinal ice extent:** We used a recent compilation of

the latitudinal extent of continental ice sheets (e.g.,  $90^\circ$  = no ice sheets) from Macdonald et al.<sup>5</sup>. This compilation is based on a literature review of the geological constraints on glaciation during the Phanerozoic, and the inferred paleogeographic extent of continental ice using updated age constraints (a full discussion of this database is described in the Supplementary Information accompanying ref.<sup>5</sup>). The time-series (units: degrees) is regular with a 1 Myr interval interpolated to 0.5 Myr.

8. **Subduction zone length:** The total length of subduction zones (including oceanic arcs) through geological time were taken from Matthews et al.<sup>11</sup>, and extracted using **pyGPlates**<sup>56</sup> at 1 Myr intervals. Spatial and temporal constraints on the distribution and extent of subduction zones are provided by geological constraints such as, for instance, ophiolites, subduction-related magmatism and the occurrence of high pressure metamorphic lithologies that are consistent with subduction processes<sup>57</sup>. As noted by Merdith et al.<sup>57</sup>, there are some similarities in the trends of subduction zone and continental arc lengths<sup>14</sup>, lending support to these independently-derived measures. The time-series is regular at 1 Myr intervals (units: km), interpolated to 0.5 Myr.
9. **Active LIP area:** We used the area of Large Igneous Provinces (LIPs) actively erupting at a particular 1 Myr time step from the compilation of Johansson et al.<sup>20</sup>. This database, which includes continental and oceanic LIPs, was compiled and digitised from the literature and their locations were reconstructed using **GPlates** software<sup>20</sup>. An underlying assumption of this time-series is that the LIPs were active for a total period of 3 Myr after their accepted eruption age. The time-series is regular at 1 Myr intervals (units: km<sup>2</sup>), interpolated to 0.5 Myr.
10. **Weatherable LIP area in the tropics:** We also use the area of LIPs (active or inactive) exposed within  $15^\circ$  of the equator at a particular 1 Myr time step<sup>20</sup>. Johansson et al.<sup>20</sup> applied paleogeographic reconstructions to discriminate between continental and oceanic LIPs in order to isolate exposed (continental) LIPs within the tropics. This regular time-series (1 Myr interval, units: km<sup>2</sup>) provides a minimum estimate of LIP area through time.
11. **Igneous Sr ratio:** We use the  $^{87}\text{Sr}/^{86}\text{Sr}$  ratio of zircon-bearing igneous rocks (i-zig) over the last 400 Ma, from the compilation from Bataille et al.<sup>16</sup> that spans 1000 Ma, to assess the relative contribution of continental igneous rock lithologies (i.e., dominantly continental volcanic arcs, which are the locus of zircon formation) to  $(^{87}\text{Sr}/^{86}\text{Sr})_{sw}$ . The authors applied a bootstrap resampling approach to correct for geographic/sampling biases in the detrital zircon record comprising 24,715 individual zircon grains. Bataille et al.<sup>16</sup> used the relationship between the  $\epsilon\text{Hf}$  compositions of zircons and the  $\epsilon\text{Sr}$  of their igneous host rocks to estimate the secular variations in the  $(^{87}\text{Sr}/^{86}\text{Sr})_{i-zig}$  through time—reflecting the changing proportion of juvenile and reworked materials generated during orogenesis. We re-ran code from Bataille et al.<sup>16</sup>, using a modified smoothing window of 5 Myr, and increment and scale

of 0.5 Myr (previously 10 Myr and 1 Myr, respectively, in Bataille et al.<sup>16</sup>). Additionally, we applied an adaptive window (decreasing in size) for data points between 5 and 0 Ma, to enable extension of the time-series to 0.5 Ma.

### 3.0. Auto- and Cross-correlations

Many of the studied variables are strongly auto-correlated and cross-correlated (e.g., due to being different proxies for the same or related processes/states). This makes it very difficult to identify dominant driving processes and their time lags. It is straightforward to compute partial autocorrelations for individual parameters—a standard approach in time-series analysis, however the multivariate case cannot always be solved. We tested whether the multivariate partial autocorrelation could be computed for our data set using an **R** implementation of the PACF<sup>58</sup> (function *acffpacf* in the *stats* package). This function computes the partial lag autocorrelation matrix  $P(s)$  of Heyse and Wei<sup>58</sup> (pp 411-414 in Wei<sup>59</sup>), where  $P(s)$  is the autocorrelation matrix between  $\mathbf{Z}_t$  and  $\mathbf{Z}_{t+s}$  after removing the linear dependency on the vectors at intervening lags  $\mathbf{Z}_{t+1}, \mathbf{Z}_{t+2} \dots \mathbf{Z}_{t+s-1}$ . The elements are normalised correlation coefficients. Based on this analysis, we concluded that the multivariate PACF<sup>58</sup> could not successfully be computed for our data.

To provide an alternative means of accounting for the combined effect of multiple parameters (at varying lags) on the variable of interest  $(^{87}\text{Sr}/^{86}\text{Sr})_{sw}$ , we developed a novel method based on conditional correlation, estimated using UNINET<sup>50</sup>. The approach we employ is similar in principle to the multivariate partial autocorrelation, but evaluates the conditional correlation for variables added iteratively to the BN at increasing time lags.

Code is written in C++ and uses the UNINET Windows COM library<sup>50</sup>. UNINET<sup>50</sup> is a software package for uncertainty analysis and dependence modelling for high dimensional distributions, originally developed for the CATS (Civil Aviation Transport Safety) project<sup>60,61</sup>. It is available as a standalone application, and as a Windows COM library (the UNINET Engine) enabling alternative programming interfaces, including but not limited to: **R**, Matlab, and Visual Studio/C++ (used here). UNINET models empirical multivariate distributions by building a joint density function from a set of inputs (data mining). Joint dependency is represented by conditional rank correlation, using the joint normal copula<sup>62</sup>.

### 4.0. Summary of the data mining algorithm

Input data are time-series for the variable of interest  $\mathbf{X}_t$  (which in this instance is  $(^{87}\text{Sr}/^{86}\text{Sr})_{sw}$ ) and the 12 predictor variables  $\mathbf{A}_t, \mathbf{B}_t, \mathbf{C}_t, \dots \mathbf{L}_t$  (observables listed in section 2.0), plus lagged values of those variables  $\mathbf{A}_{t-2.5} \dots \mathbf{A}_{t-50}$  etc. Nodes are grouped and evaluated in order of increasing lag, giving a set of observables  $(\mathbf{A}_t, \mathbf{B}_t, \mathbf{C}_t, \dots \mathbf{L}_t)$  at lag 0;  $(\mathbf{A}_{t-2.5}, \mathbf{B}_{t-2.5}, \dots \mathbf{L}_{t-2.5})$  at lag  $t-0.5$  Myr to  $t-2.5$  Myr etc., up to 50 Myr.

We construct the network by starting with the unlagged variable with the highest empirical correlation with  $(^{87}\text{Sr}/^{86}\text{Sr})_{sw}$ , then systematically search through the set of remaining predictor variables to find maximum values of conditional correlation

637 ( $C_{Cond}$ ) at increasing time lags. At each iteration we look for<sup>685</sup>  
 638 the largest  $C_{Cond}$  as this identifies the variable that individually<sup>686</sup>  
 639 provides the maximum additional information at each step. The<sup>687</sup>  
 640 variable with the largest  $C_{Cond}$  is subsequently added to the net-<sup>688</sup>  
 641 work if all of these following conditions are met: <sup>689</sup>

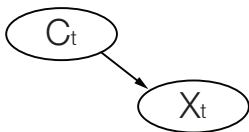
- 642 1. Its conditional correlation  $C_{Cond}$  (the correlation with  
 643  $(^{87}\text{Sr}/^{86}\text{Sr})_{sw}$ , conditional on all other variables in the net-  
 644 work) exceeds a specified confidence interval threshold.  
 645 Here we use the 99% CI, with the threshold depending  
 646 on the number of observations used to generate the time-  
 647 series for the variable in question. This results in a higher  
 648 threshold for lower resolution variables. <sup>690</sup>
- 649 2. The difference between the (unconditional) empirical rank  
 650 correlation  $C_{Emp}$  and BN (i.e., modelled) rank correlation  
 651  $C_{BN}$  with  $(^{87}\text{Sr}/^{86}\text{Sr})_{sw}$  is less than 30%. This eliminates  
 652 variables that cannot be represented accurately by the BN  
 653 (using normal copulae) and prevents such nodes affecting  
 654 the estimates of conditional dependence for subsequent<sup>696</sup>  
 655 nodes. <sup>697</sup>
- 656 3. The variable is not highly correlated (a correlation of 0.8  
 657 or greater) with any existing variables in the network (i.e.,  
 658 nodes higher up in the network hierarchy). This reduces<sup>700</sup>  
 659 the effect of collinearity. <sup>701</sup>

660 This procedure is repeated for each discrete time lag, result-<sup>702</sup>  
 661 ing in the lagged variables being either added to the network<sup>703</sup>  
 662 (in order of decreasing conditional correlation and increasing<sup>704</sup>  
 663 lag, respectively), or rejected for not meeting one of the three<sup>705</sup>  
 664 criteria above. These steps ensure the construction of a par-<sup>706</sup>  
 665 simonious model where only the most informative nodes are<sup>707</sup>  
 666 retained. We present the calculated Empirical, BN (modelled)<sup>708</sup>  
 667 and Conditional (modelled) rank correlations for each variable<sup>709</sup>  
 668 and time lag in Figure 3 and Extended Data Figure 2. <sup>710</sup>

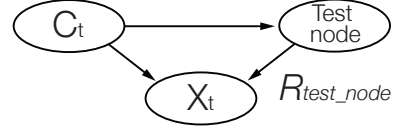
669 The computational efficiency of UNINET means that this ap-<sup>711</sup>  
 670 proach is suitable for application to large numbers (of the order<sup>712</sup>  
 671 hundreds to thousands) of nodes—greater than demonstrated<sup>713</sup>  
 672 here. <sup>714</sup>

#### 673 4.1: Itemised steps to construct the network: <sup>716</sup>

- 674 1. Generate a saturated BN using all variables (nodes) with<sup>717</sup>  
 675 lag 0 ( $\mathbf{A}_t, \mathbf{B}_t, \mathbf{C}_t \dots \mathbf{X}_t$ ) and identify the node with<sup>718</sup>  
 676 the largest empirical correlation ( $C_{Emp}$ ) with the variable<sup>719</sup>  
 677 (node) of interest  $\mathbf{X}_t$ . This node (e.g.,  $\mathbf{C}_t$ ) individually<sup>720</sup>  
 678 gives the most information about  $\mathbf{X}_t$  so it is placed first<sup>721</sup>  
 679 in the network hierarchy. The variable of interest  $\mathbf{X}_t$  al-<sup>722</sup>  
 680 ways remains last in the hierarchy, as we are interested in<sup>723</sup>  
 681 computing the probability of  $\mathbf{X}_t$  given all the other observ-<sup>724</sup>  
 682 ables. (NB: A saturated BN contains arcs linking every<sup>725</sup>  
 683 pair of nodes in the network). The first stage network is as,<sup>726</sup>  
 684 follows: <sup>727</sup>



2. Step through all the remaining nodes with lag 0 ( $\mathbf{A}_t \dots \mathbf{L}_t$ )  
 and add them one by one, as a second “test node” in the  
 network (see figure below). Calculate the conditional rank  
 correlation  $c$  for each test node in turn e.g.,  $c = C_{Cond}(\mathbf{X}_t$   
 $\mathbf{A}_t | \mathbf{C}_t)$ .



Poor fit (i.e., how well the BN can represent dependency  
 with the node of interest) is penalised by calculating  $c' = (1 - p)c$ ,  
 where  $p$  is a penalty value simply based on the absolute  
 fractional difference between the empirical and BN  
 correlations ( $C_{Emp}(\mathbf{X}_t | \mathbf{A}_t)$  and  $C_{BN}(\mathbf{X}_t | \mathbf{A}_t)$  respectively);  
 i.e., if these are the same, the penalty  $p$  is zero:

$$p = \text{abs}((C_{Emp}(\mathbf{X}_t | \mathbf{A}_t) - C_{BN}(\mathbf{X}_t | \mathbf{A}_t)) / C_{Emp}(\mathbf{X}_t | \mathbf{A}_t))$$

This prioritises inclusion of nodes that can be represented  
 most accurately by the BN.

3. Find the node that has the largest (absolute) value  $c'$   
 ( $c'_{max}$ ). If the conditional correlation  $c$  is below the spec-  
 ified confidence interval threshold set for this particular  
 node, or if  $p > 0.3$  (the BN and empirical correlations  
 differ by more than 30%), the node is eliminated and not  
 added to the network (in this case, move to step 5).
4. Reduce collinearity (high correlations between predictor  
 nodes) as follows: If the node giving  $c'_{max}$  has not already  
 been eliminated in step (3) calculate the empirical corre-  
 lation of this node with all other nodes higher in the BN  
 hierarchy (i.e., all nodes other than the node of interest,  
 $\mathbf{X}_t$ ). If this returns an empirical correlation greater than a  
 given threshold (in this case 0.8) indicating high collinear-  
 ity, the node is eliminated and not added to the network. If  
 the empirical correlations are all below 0.8, add the node  
 to the network and proceed to step (5).
5. Repeat steps (2) through (4) with all remaining lag 0  
 nodes, until they are all either added to, or eliminated from  
 the network according to the steps above.
6. Repeat steps (2) through (5) using the set of nodes with  
 lag 0.5-2.5 Myr ( $\mathbf{A}_{t-2.5}, \mathbf{B}_{t-2.5}, \dots \mathbf{L}_{t-2.5}$ ) etc., up to the  
 maximum lag (50 Myr).

Using the resulting network, we can then compute and  
 plot the conditional rank correlation for each variable at  
 increasing lag, having effectively removed both the effect  
 of shorter period lags, and other more informative predic-  
 tor variables (see Fig. 3; Extended Data Fig. 2).

Please note that an additional reference is cited in an Extended  
 Data Figure<sup>63</sup>.

#### 728 Data availability

729 All data generated or analysed during this study are provided  
 730 in the online version of this article (Supplementary Data Files  
 731 S1–S2) and in Extended Data Tables 1–2.

## 732 Source data

### 733 *Supplementary Data File S1:*

734 Time-series compilation of all data used in our network, span-  
735 ning the period from 410–0 Ma. This includes (a) the pre-  
736 dictor variables, which are: continental arc length<sup>14</sup>, suture  
737 zone length<sup>5</sup>, latitudinal extent of continental ice sheets<sup>5</sup>, con-  
738 tinental area within 20° of the tropics (this study), continen-  
739 tal area within 10° of the tropics (this study), plate tectonic  
740 fragmentation index (this study), subduction zone length<sup>11, 57</sup>,  
741 seafloor productivity (this study), atmospheric pCO<sub>2</sub> (ref.<sup>12</sup>),  
742 area of LIPs within 15° of the tropics<sup>20</sup>, eruptive area of LIPs<sup>20</sup>,  
743 <sup>87</sup>Sr/<sup>86</sup>Sr of continental igneous lithologies<sup>16</sup>; and (b) the node  
744 of interest, (<sup>87</sup>Sr/<sup>86</sup>Sr)<sub>sw</sub> (ref.<sup>15</sup>), as well as a normalised version  
745 accounting for radioactive decay of <sup>87</sup>Rb in the crust through  
746 geological time<sup>16</sup>. The records were interpolated to obtain a  
747 regular (1 Myr interval) time-series, and in cases where multi-  
748 ple values occurred within a single time stamp we used a mov-  
749 ing average with a 1 Myr window.

### 750 *Supplementary Data File S2:*

751 S2 lists the complete set of correlations for all test nodes with  
752 (<sup>87</sup>Sr/<sup>86</sup>Sr)<sub>sw</sub>. Note that C<sub>Emp</sub> = Empirical Rank Correlation;  
753 C<sub>BN</sub> = BN Rank Correlation; C<sub>Cond</sub> = Conditional Rank Corre-  
754 lation. Nodes with C<sub>Cond</sub> greater than the 99 percent confidence  
755 interval threshold (CI<sub>thresh</sub>, see the Methods for further details)  
756 were retained in the BN (highlighted in green in column F).  
757 The table of correlations includes maximum C<sub>Cond</sub> for nodes  
758 that were subsequently eliminated (shown in red).

## Code availability

The numerical modeling codes associated with this paper are available from the corresponding author (Thomas.Gernon@noc.soton.ac.uk) upon reasonable request.

50. Uninet software designed by the Risk and Environmental Modeling group, Delft University of Technology, developed by Dan Ababei, Lighttwist Software; <https://lighttwist-software.com/uninet/>.
51. Microsoft Visual Studio Technologies, Develop C and C++ applications; <https://visualstudio.microsoft.com/vs/features/cplusplus/>.
52. The R Project for Statistical Computing; <https://cran.r-project.org/>.
53. GPlates software for the interactive visualisation of plate-tectonics; <https://www.gplates.org/>.
54. M. Domeier and T. H. Torsvik. Plate tectonics in the late Paleozoic. *Geoscience Frontiers*, 5(3):303–350, 2014.
55. R. D. Müller, M. Seton, S. Zahirovic, S. E. Williams, K. J. Matthews, N. M. Wright, G. E. Shephard, K. T. Maloney, N. Barnett-Moore, M. Hosenipour, D. J. Bower, and J. Cannon. Ocean basin evolution and global-scale plate reorganization events since Pangea breakup. *Annual Review of Earth and Planetary Sciences*, 44(1):107–138, 2016.
56. PyGPlates library for GPlates functionality using the Python programming language; <https://http://www.gplates.org/docs/pygplates/>.
57. A. S. Merdith, A. S. Collins, S. E. Williams, S. Pisarevsky, J. D. Foden, D. B. Archibald, M. L. Blades, B. L. Alessio, S. Armistead, D. Plavsa, C. Clark, and R. D. Müller. A full-plate global reconstruction of the Neoproterozoic. *Gondwana Research*, 50:84–134, 2017.
58. J. F. Heyse and W. W. S. Wei. Modelling the advertising-sales relationship through use of multiple time series techniques. *Journal of Forecasting*, 4(2):165–181, 1985.
59. W. W. S. Wei. *Time Series Analysis*. Addison-Wesley, 1990.

60. B. Ale, L.J. Bellamy, R.M. Cooke, M. Duyvis, D. Kurowicka, P.H. Lin, O. Morales, A. Roelen, and J. Spouge. Causal Model for Air Transport Safety. Technical report, NLR Air Transport Safety Institute, 2009.
61. B. J. M. Ale, L. J. Bellamy, R. van der Boom, J. Cooper, R. M. Cooke, L. H. J. Goossens, A. R. Hale, D. Kurowicka, O. Morales, A. L. C. Roelen, and J. Spouge. Further development of a causal model for air transport safety (CATS): Building the mathematical heart. *Reliability Engineering & System Safety*, 94(9):1433–1441, 2009.
62. D. Kurowicka and R. Cooke. *Uncertainty Analysis with High Dimensional Dependence Modelling*. John Wiley Sons, Ltd, 2006.
63. C. R. Stern. Active Andean volcanism: its geologic and tectonic setting. *Revista Geológica de Chile*, 31(2):161–206, 2004.

## Acknowledgements

This study was supported by a Natural Environment Research Council (NERC) grant (NE/R004978/1) to T.G., which also supported T.H. and M.P. T.G. and T.H. were supported by The Alan Turing Institute under the EPSRC grant EP/N510129/1.

## Author contributions

T.G. conceived the idea, led the study, interpreted the data and prepared the manuscript and figures. T.H. performed the modeling, designed the network and carried out the analysis, with input from T.G. A.M. calculated the seafloor production rates, and both A.M. and D.M. provided support with *GPlates* and *pyGPlates*. M.P. and C.B. provided support with Sr isotope interpretation, and C.B. provided normalised Sr data. G.F. provided CO<sub>2</sub> data and both G.F. and E.R. assisted with paleoclimate interpretation. T.G. wrote the manuscript with input from all co-authors.

## Competing interests:

The authors declare no competing interests.

## Additional information

**Supplementary information** is available for this paper at <https://doi.org/10.1038/s12345-111-2222-3>.

**Correspondence and requests for materials** should be addressed to T.G.

**Reprints and permissions information** is available at <http://www.nature.com/reprints>.

# Figures

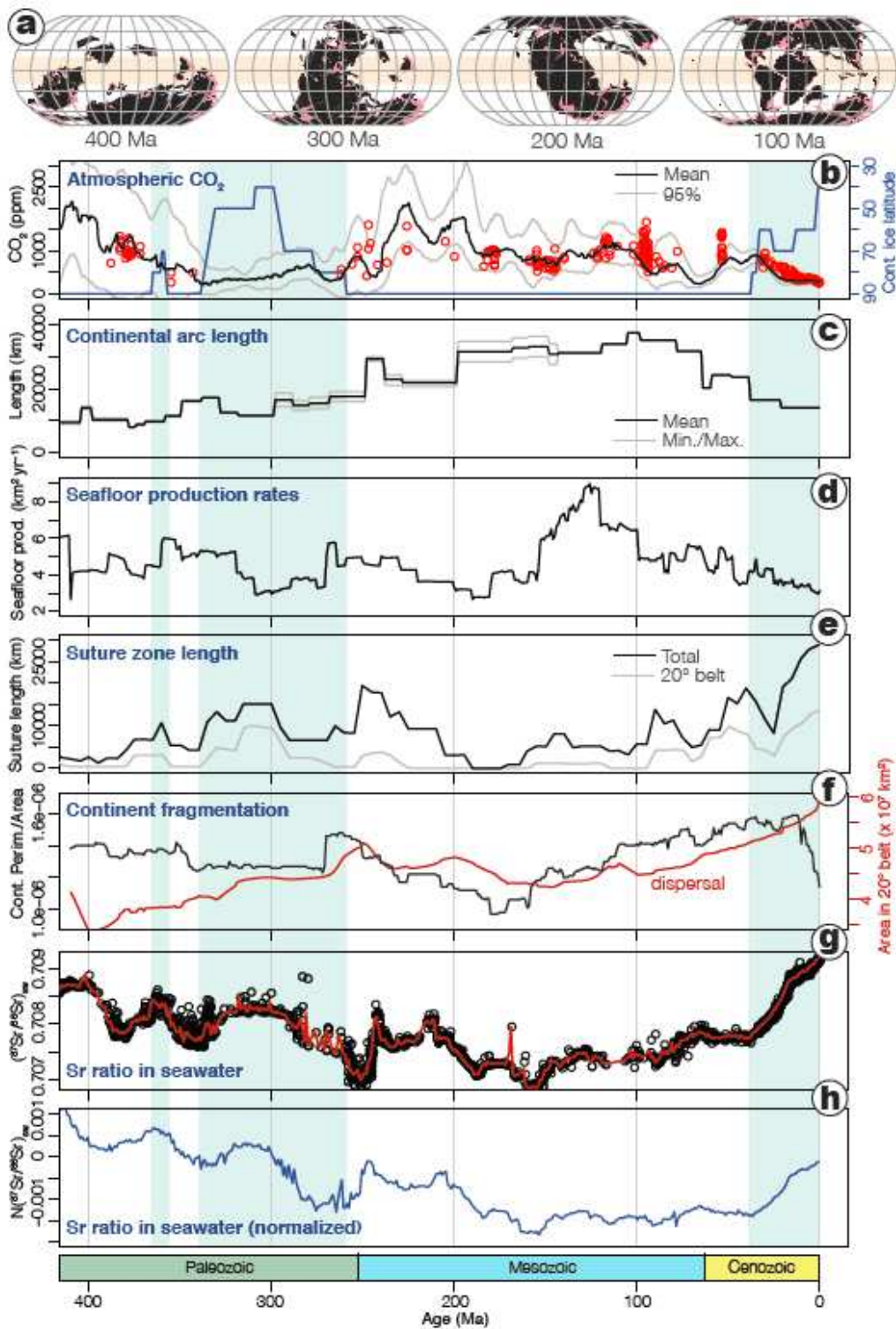


**Figure 1**

Tectonic, atmospheric and ocean chemical changes over the past 400 Myr j a, Continental distribution 11 with continental landmasses shown in pink, present-day coastlines in black, and the tropics ( $\pm 20^\circ$  of the equator) in beige; b, atmospheric CO<sub>2</sub> concentration (multi-proxy, black line) 12, and phytane-based

estimates in red 13; continental ice latitude 5 is shown as the blue line (blue shaded regions denote glaciations); c, continental arc length 14; d, seafloor production rates (Methods); e, suture zone lengths 5; f, fragmentation index (i.e., continental perimeter/area, as black line), and total area of continents in the tropics (red line); g,  $(^{87}\text{Sr}/^{86}\text{Sr})_{\text{sw}}$  from marine carbonates 15, calculated as a  $\pm 0.25$  Myr window in red; h, normalised  $(^{87}\text{Sr}/^{86}\text{Sr})_{\text{sw}}$  curve removing the signal caused by radioactive  $^{87}\text{Rb}$  decay in the crust 16. Note: The designations employed and the presentation of the material on this map do not imply the expression of any opinion whatsoever on the part of Research Square concerning the legal status of any country, territory, city or area or of its authorities, or concerning the delimitation of its frontiers or boundaries. This map has been provided by the authors.

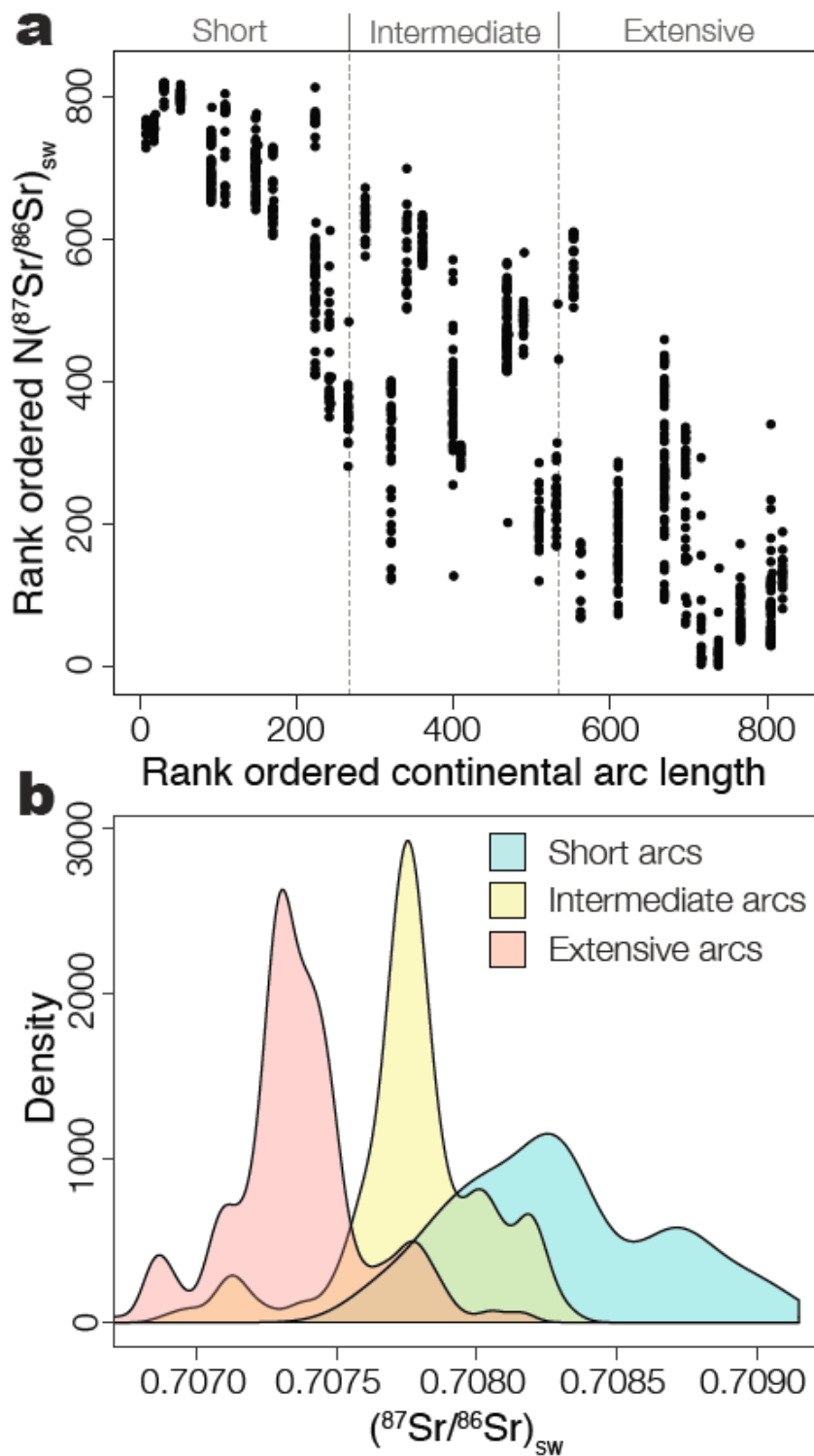


**Figure 2**

Effects of continental arc extent on the strontium isotopic composition of seawater j a, Ranked ordered normalised  $(^{87}\text{Sr}/^{86}\text{Sr})_{\text{sw}}$  16 versus ranked continental arc length (see Extended Data Fig. 3 for the non-normalised and unranked versions). Note that the smallest value that occurs in the data set is ranked 1. b, Probability density for continental arc length 14, identifying short (<16,100 km), intermediate (16,100–29,300 km), and extensive ( $\geq$ 29,300 km) arcs (note: these divisions denote approximately equal

quantiles); the distributions show that extensive continental arc systems favour low  $(^{87}\text{Sr}/^{86}\text{Sr})_{\text{sw}}$ , and vice versa.

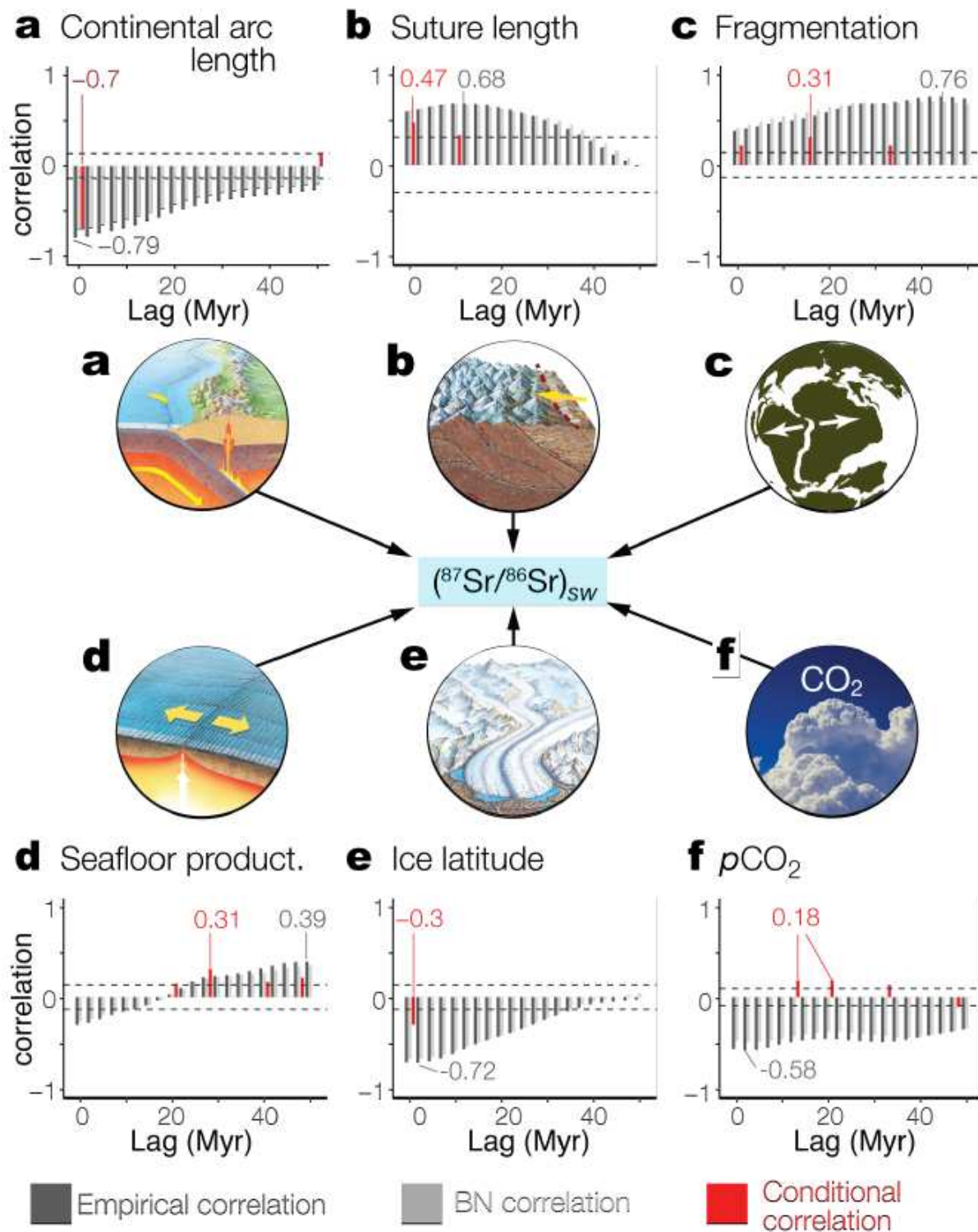


**Figure 3**

Simplified network structure showing key geological processes and correlations with seawater Sr  
 Graphical representation of our network, showing how the six dominant variables (a–f) influence  $(^{87}\text{Sr}/^{86}\text{Sr})_{\text{sw}}$  (Extended Data Fig. 2). The plots summarise the relationships between the relevant

variable and  $(^{87}\text{Sr}/^{86}\text{Sr})_{\text{sw}}$  for all time steps in our analysis ( $n = 360$ ). The plots show CEmp, CBN, and CCond, at time lags from 0 to 50 Myr in 2.5 Myr intervals. A lag of 0 means the relevant process is occurring within the same 1 Myr time-step. The values shown in gray on the plots are the highest value of CEmp; if each process were considered in isolation this value would represent the dominant time lag. However due to autocorrelation and joint dependence, the dominant processes and time lags can be better identified by peak CCond (red). The horizontal dashed lines denote 99% confidence intervals.

## Supplementary Files

This is a list of supplementary files associated with this preprint. Click to download.

- [NGS20201002584TS1.csv](#)
- [NGS20201002584TS2.xlsx](#)
- [NGS20201002584TExtendedData.pdf](#)